PAPER Nr. : 14

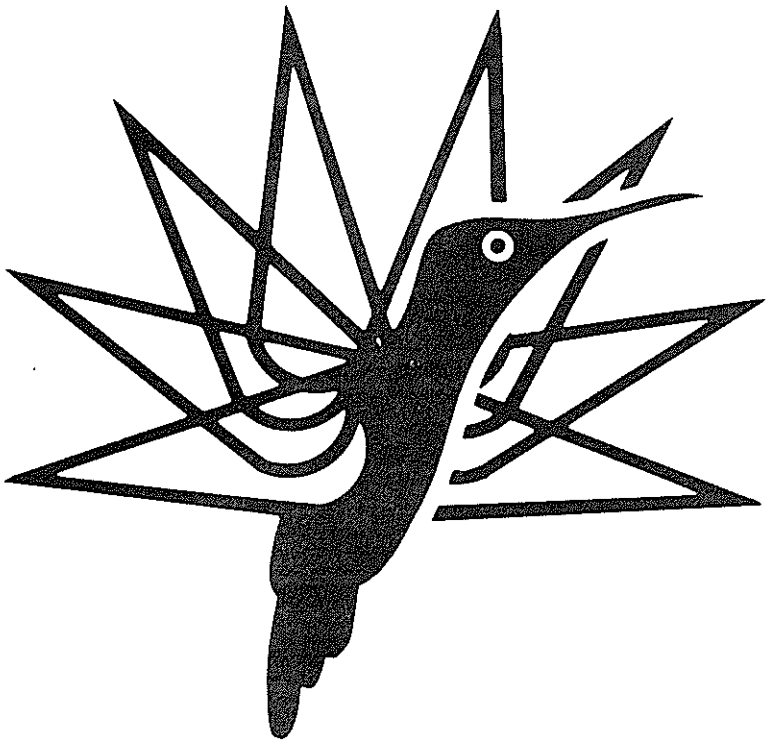

CORRELATION OF PUMA AIRLOADS – EVALUATION OF CFD PREDICTION METHODS

Roger C. Strawn
U. S. Army Aeroflightdynamics Directorate
Moffett Field, California, USA

Andre Desopper
Office National d'Etudes et de Recherches Aerospatiales
Chatillon, France

Judith Miller and Alan Jones
Royal Aerospace Establishment
Farnborough, England

FIFTEENTH EUROPEAN ROTORCRAFT FORUM

SEPTEMBER 12 - 15, 1989 AMSTERDAM

CORRELATION OF PUMA AIRLOADS – EVALUATION OF CFD PREDICTION METHODS

Roger C. Strawn
U. S. Army Aeroflightdynamics Directorate
Moffett Field, California, USA

Andre Desopper
Office National d'Etudes et de Recherches Aerospatiales
Chatillon, France

Judith Miller and Alan Jones
Royal Aerospace Establishment
Farnborough, England

ABSTRACT

A cooperative program has been undertaken by research organizations in England, France, Australia and the U. S. A. to study the capabilities of computational fluid dynamics codes (CFD) to predict the aerodynamic loading on helicopter rotor blades. The program goal is to compare predictions with experimental data for flight tests of a research Puma helicopter with rectangular and swept-tip blades. Two topics are studied in this paper. First, computed results from three CFD codes are compared for flight-test cases where all three codes use the same partial inflow-angle boundary conditions. Second, one of the CFD codes (FPR) is iteratively coupled with the CAMRAD/JA helicopter performance code. These results are compared with experimental data and with an uncoupled CAMRAD/JA solution. The influence of flowfield unsteadiness is found to play an important role in the blade aerodynamics. Alternate boundary conditions are suggested in order to properly model this unsteadiness in the CFD codes.

LIST OF SYMBOLS

c	= rotor chord length
C_l	= lift coefficient
C_m	= pitching moment coefficient
C_p	= pressure coefficient
C_T/σ	= ratio of rotor thrust coefficient to solidity
M_T	= hover tip Mach number
r	= spanwise distance along the rotor
R	= radial distance to the rotor tip
t	= time

x = chordwise distance along the rotor

α_p = partial angle of attack provided to the CFD codes

μ = rotor advance ratio

ψ = rotor azimuthal angle, deg.

θ = blade cyclic pitch angle, deg.

1. INTRODUCTION

Accurate methods for flow prediction on helicopter rotors are an important part of the rotor design process. Examples of comprehensive helicopter prediction codes are given in Refs. 1-4. For these codes, typical aerodynamic models consist of lifting-line methods for the blade aerodynamic loads. Sectional lift, moment and drag are based on 2-D experimental airfoil data. Approximate methods are then used to correct for unsteady and three-dimensional effects near the blade tip. The rotor wake is modeled with discrete vortex segments that are tracked in a Lagrangian framework. Wake-induced inflow to the rotor disc is computed with a Biot-Savart integration. The rotor-wake, aerodynamics and dynamics solutions are coupled together in an iterative trim solution in order to balance the forces for the entire helicopter.

Alternatives to lifting-line models for blade aerodynamics are computational fluid dynamics schemes (CFD) that compute the full three-dimensional transonic flow around rotor blades. These methods typically solve the Navier-Stokes, Euler, or potential-flow equations. CFD methods have the advantage over other methods because they are designed to accurately model the three-dimensionality and the transonic flow nonlinearities that are associated with high-speed advancing rotors. The disadvantage of these methods is that computer speed and storage requirements limit the size of the computational domain. The complexities of resolving the rotor wake system and blade dynamics are typically beyond the capabilities of current CFD codes.

To surmount these problems, hybrid approaches have been developed that replace the lifting-line aerodynamic models in rotor comprehensive codes with aerodynamic loads that are computed with CFD. The advantage is that the CFD-computed aerodynamic loads should more accurately model unsteady transonic effects and blade three dimensionality. In addition, the rotor-wake and dynamics can be modeled by simple boundary conditions to the CFD code. This type of hybrid coupling approach was first developed by Tung et al. [5] who iteratively coupled the CFD computed lift from a small-disturbance potential code to the CAMRAD comprehensive analysis [1,2].

Since then this same hybrid coupling procedure has been used with a number of different CFD methods and comprehensive rotorcraft codes [6-9]. Typically these efforts have focused more on the development of the CFD methods than on the details of the comprehensive analyses and CFD coupling scheme. This makes it difficult to compare the various methods because comparisons between the CFD codes were not always made for the same cases and conditions. Also, it has typically been difficult to evaluate the different comprehensive rotorcraft codes since they too have not been tested for similar cases. Finally, it is always difficult to obtain accurate flight-test data to validate the various prediction methods.

In order to resolve some of these issues, a cooperative research program has been undertaken between organizations in the United States, the United Kingdom, France, and Australia. The objective is to better understand the strengths and limitations of

various computational approaches for the prediction of rotor airloads. This was done by comparing the predictions from several computational schemes with airloads data obtained in the flight test of an AS 330 Puma with modified blade tips.

The Puma mixed rotor system consists of both swept and rectangular tips as shown in Fig. 1. Pressure data were simultaneously recorded for both the swept and the rectangular-tip blades during the flight tests. These flight-test cases were chosen because the high-speed forward flight and blade three dimensionality provide challenging cases for aerodynamic prediction codes. More detailed descriptions of the Puma flight tests are given in Refs. 10 and 11.

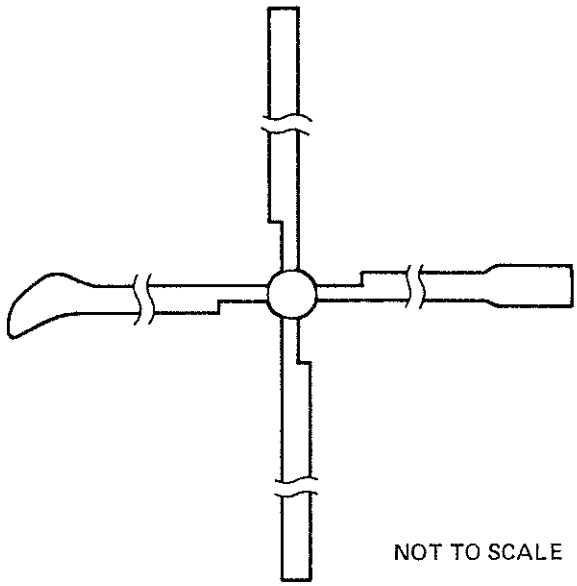

Fig. 1 Puma mixed bladed rotor configuration.

A workshop was held at RAE-Farnborough in May 1988 to compare the CFD and comprehensive lifting-line aerodynamic predictions for the Puma flight-test cases and to assess the relative strengths and limitations of each. This paper and its companion paper "Correlation of Puma Airloads – Lifting-Line and Wake Calculation" will examine the major questions that resulted from the workshop and summarize the substantial work that has been done subsequent to the workshop. The purpose of these papers is to address the following questions.

1. How good are the experimental data? Are they suitable for validation purposes?
2. How well do the lifting-line/wake methods predict the airloads measured on the Puma? Can limitations in modeling capabilities be identified?
3. Independent of the CFD predictive capability with respect to the experimental data, how well do they compare with each other? What advantages are obtained as the analysis sophistication increases from the quasi-steady small-disturbance theory to the unsteady small-disturbance theory to the full-potential model?
4. How satisfactory are the methods used to calculate the inflow for the CFD methods? How important are the differences between simply prescribing the inflow (uncoupled) and iterating between the lifting-line/wake and CFD methods (coupled)?
5. How satisfactory are the CFD methods for airloads prediction? Despite their dependence upon the lifting-line/wake methods for the correct modeling of the inflow can they provide useful physical insight?

This paper will primarily address questions 3 through 5 while the companion paper will examine questions 1 and 2. Specifically, this paper will first compare results from three CFD methods for several of the Puma flight-test cases. The same prescribed inflow boundary conditions will be used for each code. The objective will be to answer question 3 in the above list. Next, the paper will take one of the CFD codes and iteratively couple its computed lift to the CAMRAD/JA comprehensive helicopter code [12]. Results will be presented and compared to the Puma flight-test data. The iterative coupling procedure and its influence on the final set of results will be examined in detail. Results from this study will address questions 4 and 5 in the list above.

2. DESCRIPTION OF THE CFD CODES

RAE TSP Method

The RAE Transonic Small Perturbation code (TSP) solves the three-dimensional quasi-steady small-disturbance potential equation for helicopter rotor blades. The equation is written in nonconservative form and discretized with the streamwise derivatives switched from central to upwind differences in regions of supersonic flow. The wake is assumed to be a plane vortex sheet skewed in the direction of the resultant free-stream flow. Jump conditions on the velocity potential are imposed across the vortex sheet. Boundary conditions at the far field are set to free-stream values.

The difference equations are solved by an iterative relaxation technique with sweeps in each of the coordinate directions at each iteration step. A grid sequencing method using both coarse and fine grid solutions is used to speed up convergence. Further details of the code and early computed results can be found in Ref. 13. More recent work has been concerned with improvements in the grid, and inclusion of some of the terms in the differential equation which were originally considered negligible.

The grid for the Puma cases is generated algebraically and a total of 105,600 grid points are used: 60 in the chordwise direction, 44 radially, and 40 vertically. On the blade surface there are 31 points in the chordwise direction, 31 and 35 in the spanwise direction for the rectangular and swept-tip cases respectively. The outer boundaries of the computational region are at infinity. For the forward-flight Puma cases, a separate quasi-steady calculation was performed at each azimuthal station required. A total quasi-steady calculation consisting of grid generation, 150 iterations on the coarse grid, and 150 iterations on the fine grid requires about 170 CPU minutes on a DEC VAX 11/780.

ONERA TSD Method

The unsteady transonic small-disturbances method (TSD) was developed ten years ago in a cooperative effort by the Office National d'Etudes et de Recherches Aerospatiales (ONERA) and the U. S. Army Aeroflightdynamics Directorate (AFDD) at Ames Research Center. The computer code solves a conservative form of the unsteady, three-dimensional transonic small disturbance potential equation for rotor blades of nearly arbitrary planform.

The TSD code originally solved a form of the small-disturbance potential equation that was obtained by neglecting some of the spanwise terms in the equation since they are typically small, especially in cases with transonic flow near $\psi = 90°$ azimuth. Details of the method are given in Refs. 14 and 15.

Significant improvements to the original TSD code are described by Desopper [16]. This improved version of the code now includes all of the terms in the spanwise direction with no approximations. These modifications have improved both the stability of the method and also the computed results for non-rectangular blades.

For the Puma cases, the total number of mesh points used was 48300; 70 chordwise, 23 spanwise (16 on the blade) and 30 in the vertical direction. The outer boundaries of the computational domain were 9 chords upstream and 6 chords downstream, from 0.5 R to 1.5 R in the spanwise direction and 6 chords above and below the blade. The solution moved forward 1° of rotor azimuth per time step and the computing time on a CRAY XMP machine for a full 360° cycle was 850 CPU seconds.

U. S. Army FPR Method

The Full-Potential Rotor code (FPR) solves the unsteady, three-dimensional, full-potential equation in strong conservation form. The code employs a finite-difference scheme with first-order backward differencing in time and second-order central differencing in space. The temporal density derivative is locally linearized about the old time levels in a manner that preserves the conservative form. Stability in regions of supersonic flow is obtained by biasing the density calculation in the upwind direction.

A spanwise series of parallel O-grids are used for the basic grid system. Rotor flows are computed by assigning an appropriate rotational coordinate velocity to each grid point. As a result, the rotor and the attached finite-difference grid move through still air. On the surface of the blade, a transpiration velocity condition is used to simulate angle-of-attack conditions (including wake-induced inflow angles). At the outer radial boundary of the O-grid, a nonreflection boundary condition is used to prevent the accumulation of numerical disturbances.

Typical grid sizes for the calculations used for the Puma calculations are 80 points in the chordwise direction, 25 in the spanwise direction and 25 in the direction normal to the rotor surface. Figure 2 shows a top view of the FPR grid for the swept-tip Puma

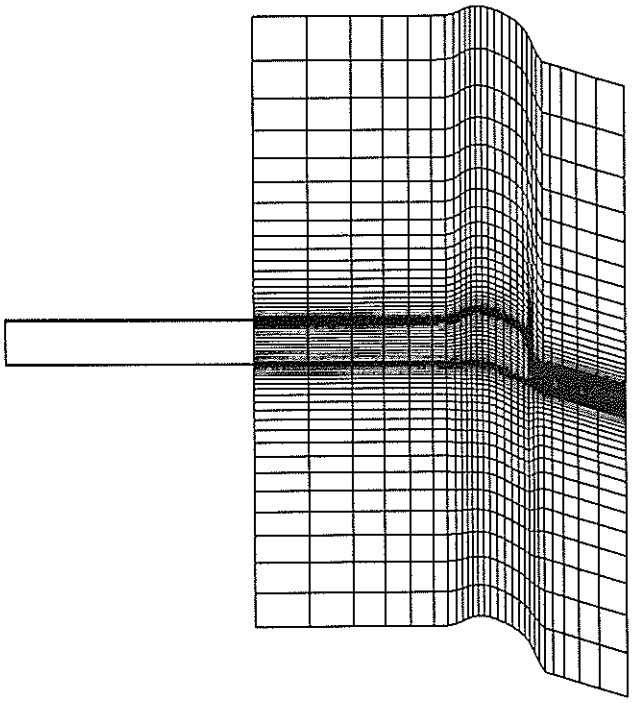

Fig. 2 Top view of the FPR grid for the swept-tip Puma calculation.

blade. The finite-difference grid extends approximately 7 chords inward from the rotor tip and two chords outward from the tip in the spanwise direction. The outer radial boundary of the O-grid is located 5 chords from the surface of the blade. Constant time steps were used corresponding to 0.25° of rotor azimuthal angle per time step. Unsteady calculations for a complete 360° of rotor azimuth required approximately 1800 CPU seconds on a CRAY XMP computer system.

A more complete description of the Full-Potential Rotor Code can be found in Refs. 17 and 18. Significant improvements to the differencing algorithm in FPR have recently been made and these are detailed in Ref. 19. This improvements increase the accuracy and stability of the solution algorithm and have been used for all of the Puma computations. Also discussed in Ref. 19 are the inclusion of viscous effects in the code and the calculation of rotor drag, torque and power.

3. TEST CASES FOR THE CFD METHODS

The three CFD prediction schemes can be compared to each other by examining the computed results from five test cases in detail. For the first three test cases the RAE supplied partial inflow angles to the CFD codes using the RAE/WHL rotor loads analysis code [3]. These partial inflow angles are implemented as an effective twist distribution at each blade azimuth that represents the influence of the far-wake and rotor dynamics. Further details on this partial inflow angle boundary condition are given in Section 5 of this paper. The important thing to keep in mind is that all three codes are compared with consistent partial inflow angle boundary conditions.

The five computed test cases can be described as follows.

1. Rectangular blade - Baseline rectangular blade case, $M_T = 0.6225$, $\mu = 0.3761$, $C_T/\sigma = 0.0798$, partial inflow angles provided by the RAE/WHL rotor loads analysis code.
2. Swept-tip blade - Swept-tip Puma blade with the same flight conditions as the rectangular blade case number 1. Partial inflow angles are provided by the RAE/WHL analysis.
3. Swept-tip blade - A swept-tip blade with slightly different flight conditions than cases 1 and 2. In this case, $M_T = 0.6244$, $\mu = 0.3813$, and $C_T/\sigma = 0.0799$. This case differs from case 2 in that all four rotor blades have swept tips. Flight-test cases 1 and 2 used a mixed combination of rectangular and swept blades. Once again, partial inflow angles were provided by the RAE/WHL analysis.
4. Swept-tip blade - This case is identical to flight-test case 2 except that the specified inflow angles are replaced by a uniform 2° angle of attack along the blade.
5. Rectangular-tip blade - This case is identical to flight-test case 1 except that the specified inflow angles are replaced by a uniform 2° angle of attack along the blade.

Initially, cases two and three were proposed because it was suspected that the analysis would show significant differences between a flight-test with only one swept-tip blade and a case where all four blades are swept. This turned out not to be the case however and the RAE /WHL performance analysis showed little difference between the two cases, and this was confirmed by the experimental data. As a result, all of the CFD predictions for case two are very similar to those for case three. This discussion will therefore not include case three in the detailed study of CFD-computed results.

In cases 1, 2 and 3 the CFD methods predicted the sectional lift to be significantly lower than the experimental data. These lift discrepancies are caused by low partial inflow angles that were provided to the codes from the RAE/WHL performance analysis. This result led to subsequent development of both the RAE/WHL and CAMRAD models for the PUMA to the improved standard reported in Ref. 20, which also includes a detailed discussion of the partial inflow calculations. These low partial inflow angles mean that it is not particularly useful to compare the CFD results directly to experimental data. All three of the CFD methods have been run with the same partial angles however, so it is still useful to compare them to each other.

As a consequence of the low partial inflow angles input to the codes, the first three computed cases do not show the strong shocks on the advancing side of the rotor that are seen in the experiment. Since the ability of the CFD codes to predict unsteady shock motion was an important issue in these comparisons, cases four and five were added to the list of computations. Although these cases do not represent any real flight conditions, they give an opportunity to compare the different CFD codes where significant shocks are present on the advancing side of the rotor disk.

The next part of this paper will present a selected portion of the results from the various CFD methods. Rather than go through the results for each case, representative figures will be shown that highlight important issues for the CFD codes. A more complete collection of the computed results is contained in the Final Report from the May 1988 workshop, currently in preparation.

4. CFD RESULTS AND DISCUSSION

Figure 3 shows predicted sectional lift results for cases 1 and 2. The computed results from the three CFD codes show good agreement, particularly for the rectangular-tip case 1. This agreement in lift between the codes is encouraging since lift is a major quantity of engineering importance. The largest discrepencies between the three predictions is seen for the swept-tip at 95% radius. Here the TSP code shows lower lift in the first and fourth azimuthal quadrants than either the FPR or TSD results. All three codes show good agreement in the second azimuthal quadrant and the TSD code shows higher lift in the third quadrant than either the TSP or FPR codes. The disturbance in the TSD and FPR results near $\psi = 280°$ is due to a slope discontinuity in the partial

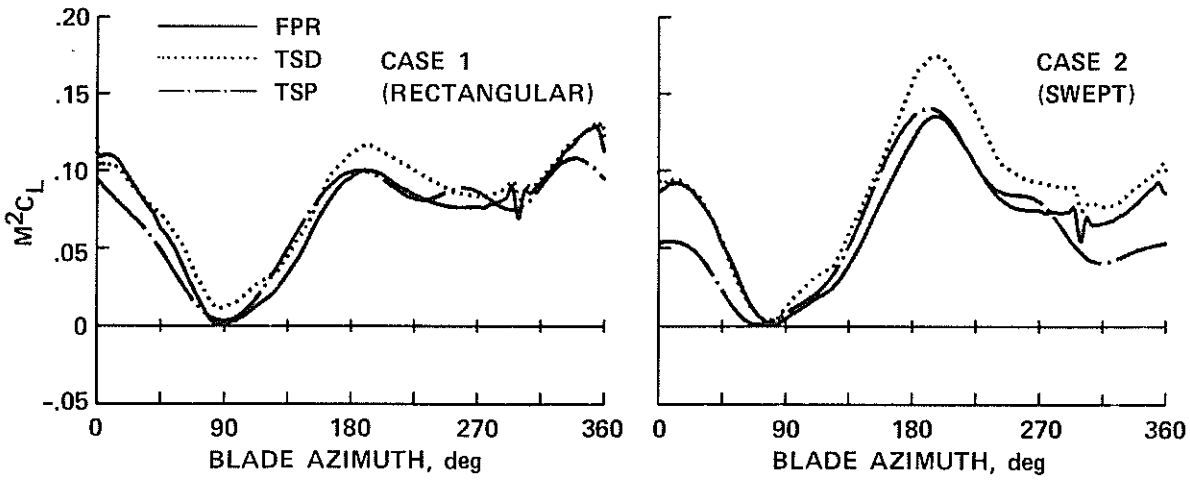

Fig. 3 Time histories for lift for test cases 1 and 2, $r/R = 0.95$.

inflow angles corresponding to a blade-vortex interaction predicted by the RAE/WHL performance code. This disturbance does not appear in the TSP results because they were computed at individual discrete azimuthal angles.

The results shown in Fig. 3 are fairly typical of the comparisons that are seen for lift in all five of the test cases. The rectangular cases show good agreement between all of the codes while some discrepancies are seen in comparisons between the swept-tip cases. In general, the lift comparisons are the least sensitive measure of differences between the three CFD codes.

The issues of planform three dimensionality and transonic flow are addressed in Fig. 4. Here Mach contours are shown for the swept-tip case 4 at 90° azimuthal angle. All three codes show a strong shock inboard of the tip with a decrease in shock strength at the start of the forward sweep. They also show about the same area and shape of the supercritical flow region. The only significant difference between the three contour plots is in the supercritical region just outboard from the start of the forward sweep. Here, all three codes predict slightly different shapes in the supercritical Mach number contours. Once the backward sweep begins to take effect, the three results look very similar.

More detailed differences between the three codes in regions of transonic flow are seen in Fig. 5. This is a rectangular-tip case with the strongest shocks in all cases. In fact, not much difference was seen in the transonic flow modeling of the codes until the advancing-side shock became this strong. At $\psi = 90°$ the TSP result shows a shock wave that is further forward than either of the other codes. This is probably due to a lack of conservation in the TSP algorithm. The FPR and TSD codes show excellent

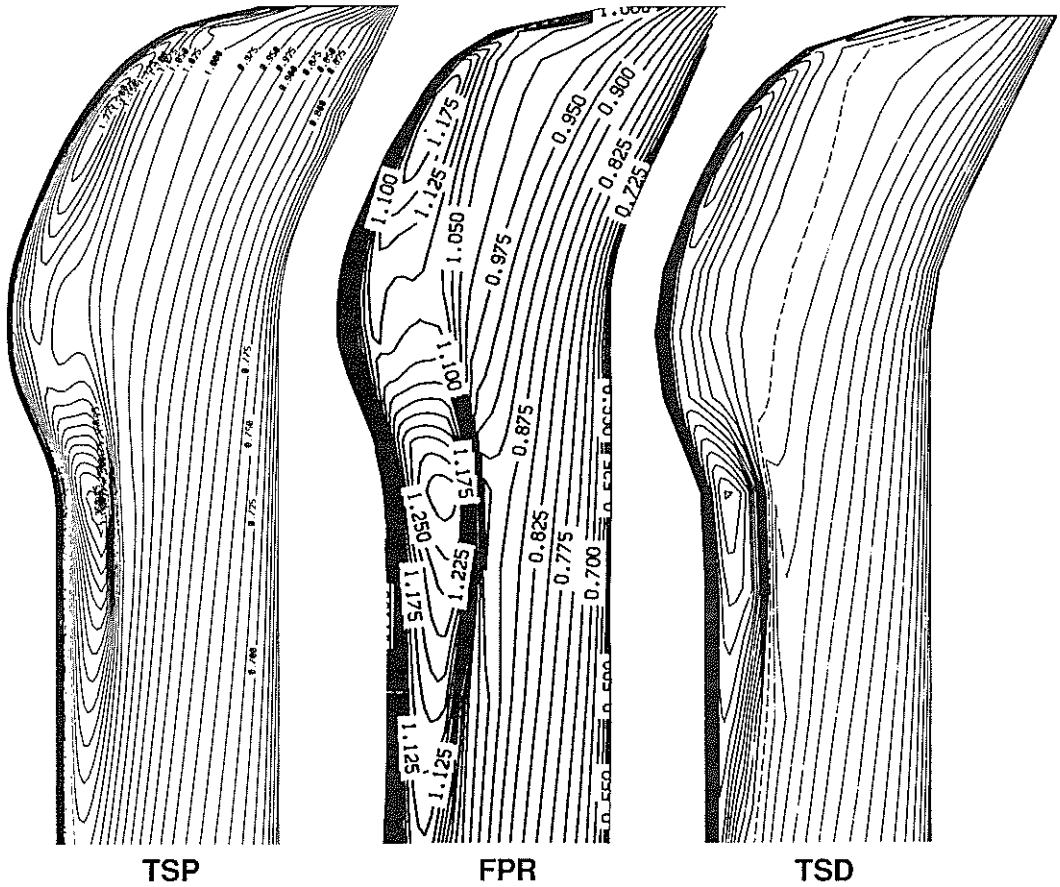

Fig. 4 Upper surface Mach contours at $\psi = 90°$ for test case 4.

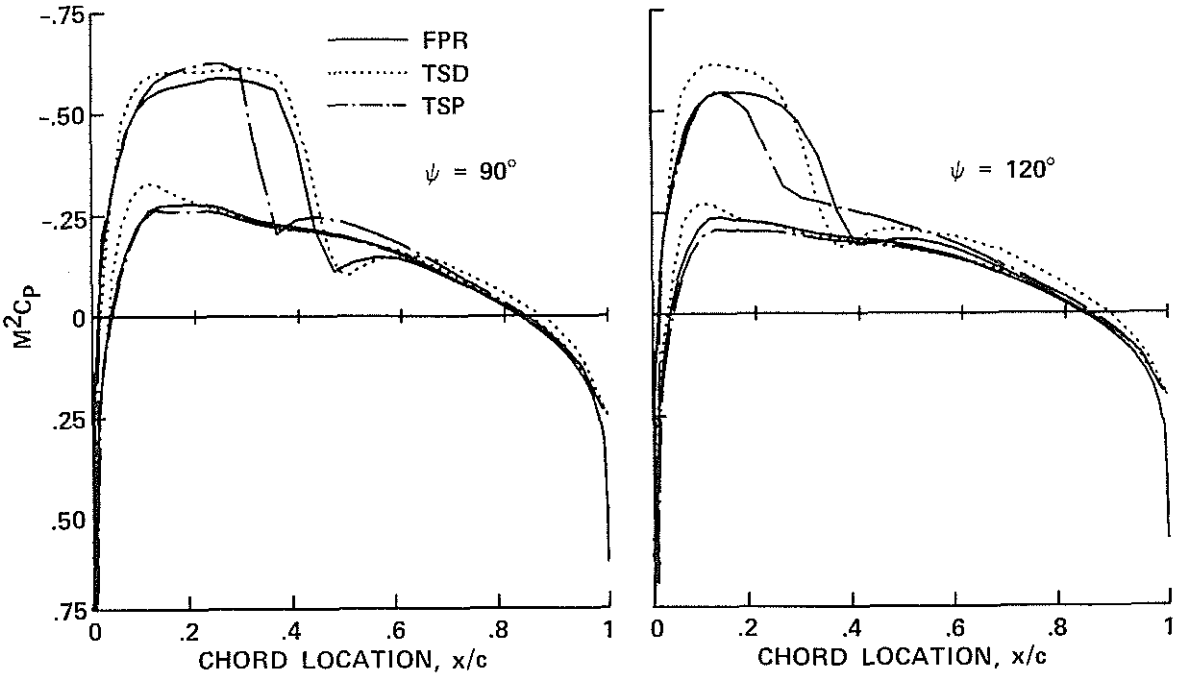

Fig. 5 Transonic surface pressures at $r/R = 0.95$ for test case 5.

agreement on upper surface shock location and strength. The lower-surface pressure for the TSD code shows more leading edge expansion than either the FPR or TSP results.

At $\psi = 120°$ in Fig. 5, significant transonic unsteadiness is present as the shock weakens in the second quadrant. Here, the maximum discrepancies are seen between all three predictions. The TSP calculation shows a shock wave that is further forward than either of the other codes, primarily because the TSP algorithm is quasi-steady. The unsteady effect on shock motion is to delay the decay of the shock wave in the second quadrant of the rotor disc. A quasi-steady code cannot model this phenomenon and is expected to show a more rapid shock decay. The FPR and TSD results again show good agreement on shock location but the FPR code shows less expansion near the leading edge of the blade. There is good agreement in the leading edge expansion region between the FPR and TSP results.

One of the important issues for the CFD codes is their ability to compute high-lift solutions on the retreating side of the rotor disk. Fig. 6 shows high-lift chordwise pressure distributions at $\psi = 270°$ for both the rectangular and swept tip (cases 1 and 2). The discrepancies between the codes in the leading edge region are consistent with the approximations in the small-disturbance potential equation. These approximations lead to an underestimation of the flow expansion around the leading edge of an airfoil in low-speed, high-lift conditions.

This trend is confirmed for the retreating-side results in Fig. 6 which show both small-disturbance codes with lower leading-edge lift than the FPR code. It is surprising that the TSP code shows more leading edge expansion than the TSD code at $\psi = 270°$ while the reverse was true on the advancing side in Fig. 5. This seems to rule out a difference in leading edge grid resolution as a cause for the differences in leading edge expansion for the TSD and TSP codes. The TSD result shows less lift at the leading edge than either the TSP or FPR codes but more lift at the trailing edge. This will tend to balance out when calculating integrated lift for the blade. It has more significant

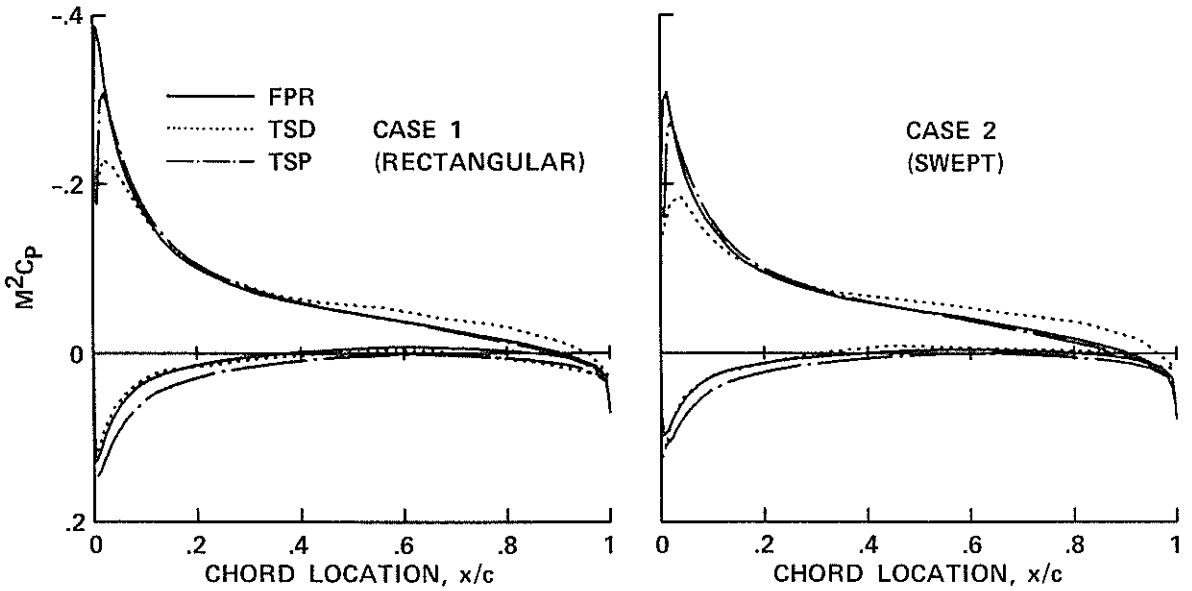

Fig. 6 Retreating side high-lift surface pressures for test cases 1 and 2, $r/R = 0.95$, $\psi = 270°$.

effects on the moment calculation however, tending to give the TSD result a larger nose-down moment than either of the other two codes.

Moment comparisons for the three codes are shown in Fig. 7. As discussed above, the TSD result shows lower moment values (more nose down) on the retreating side than either the FPR or TSD code. This is particularly true for the swept-tip case 2. The FPR code shows higher moment values than either of the other two codes for all azimuthal angles. In general there is poor agreement between the three codes for pitching moment predictions. This is not too surprising since the pitching moment is a difficult and sensitive quantity to predict accurately and subtle differences in chordwise surface pressure distributions can lead to large differences in the integrated pitching moments.

One of the major questions to be addressed in this paper is, "What level of CFD modeling is required to accurately compute transonic three-dimensional rotor geometries?" The answer to this question is not clear-cut. It is difficult to determine whether

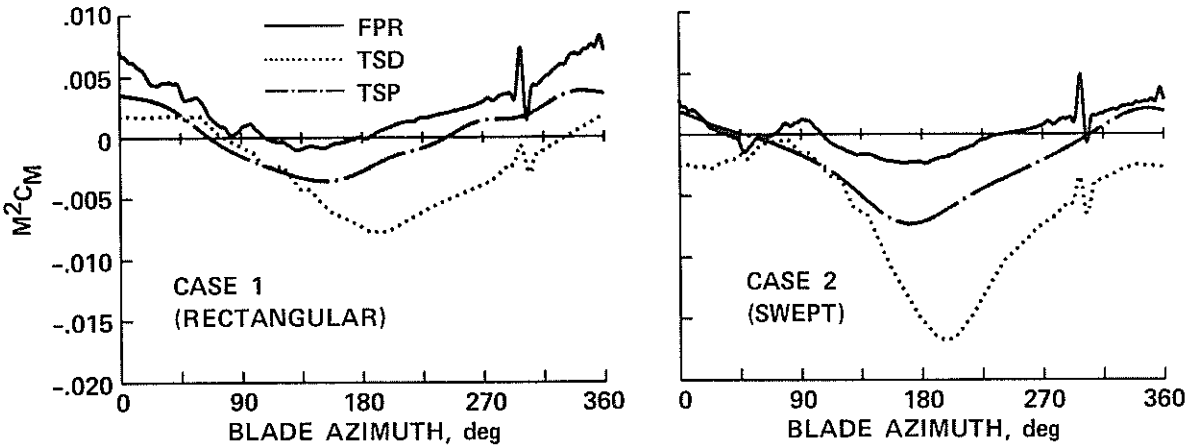

Fig. 7 Time histories for moment for test cases 1 and 2, $r/R = 0.95$.

any calculation method is superior since none of the computations showed good agreement with the experimental data. However it is possible to draw some conclusions from the comparison of the three methods to each other.

All three of the codes showed good agreement on sectional lift coefficients and the qualitative effects of three-dimensional blade-tip shapes. If computed sectional lift coefficients are the only desired output from the CFD codes, then they all give similar results for the various test cases. This is because the pressure integration process for lift smooths out individual differences in the surface pressures.

On the other hand, if drag, pitching moments or detailed surface pressures for acoustics are required, then significant individual differences exist between the three CFD analyses. These differences are difficult to generalize and seem to be dependent on the particular test case. In general however, errors in shock location will show up as large discrepancies in inviscid wave drag and advancing-side torque. Errors in leading or trailing edge pressures will show up in both the the drag and moment predictions.

The full-potential equation in the FPR code is the most rigorous theoretical model out of the three methods, and should give more accurate results than the small-disturbance codes. This is particularly true near the rotor leading edge where high gradients exist in geometry and surface pressures. One would expect to see these effects on the retreating side of the rotor disk where high inflow angles cause large suction peaks near the rotor leading edge.

The other clear difference between the three codes is that the TSP method is quasi-steady while the FPR and TSD codes are fully unsteady. The assumption of quasi-steady flow in the TSP code breaks down when there is significant unsteady transonic flow over the rotor. This often occurs in the second quadrant of the rotor disk. Outside of this region however, the flowfield unsteadiness does not seem to cause major differences between the three codes in the Puma test cases.

5. FPR AND CAMRAD/JA COUPLED SOLUTION METHOD

In order to examine more closely the role of the CFD methods in the prediction of helicopter flight-test data a fully coupled solution was performed between the CAMRAD/JA performance code [12] and the U.S. Army FPR code. The CAMRAD/JA and FPR codes were chosen as representative performance and CFD codes because the first author of this paper had easy access to both codes. Puma flight-test case 3 was chosen for the solution because we wanted to study the iterative coupling scheme for a swept-tip blade and also because the uncoupled CAMRAD/JA results for this case were in good agreement with the experimental data (see Ref. 20).

The iterative coupling scheme between the two codes was developed by Tung et al. [5] and is shown in the diagram in Fig. 8. An initial solution with CAMRAD/JA is performed and partial inflow angles (α_p) are provided to the CFD code. The partial inflow angles are functions of both span and blade azimuthal angle. They represent the inflow to the blade due to cyclic pitch, blade flapping and dynamics, and rotor wake. They are called partial angles because the inflow effects of the near-wake, contained in the CFD domain, have been removed. An example of this near-wake region is shown by the FPR grid in Fig. 2. The reason that the CAMRAD/JA wake effects are removed in this region is because the near-wake is also calculated by the CFD code. Its effect would be redundant if it were included in both CAMRAD/JA and the FPR code.

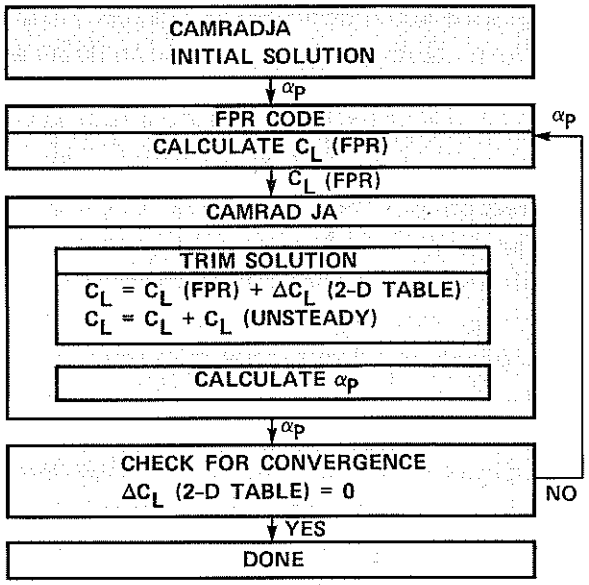

Fig. 8 Iterative coupling scheme between CAMRAD/JA and FPR.

Given the partial inflow angles from the CAMRAD/JA analysis, the FPR code computes the unsteady lift values as functions of span and azimuthal angle. These lift values are then provided to the CAMRAD/JA analysis and used in its trim solution. Note that the FPR code sits outside of the CAMRAD/JA trim loop. Because the CAMRAD/JA code must dynamically update its C_l values many times throughout the trim loop, it would be impractical to run the CFD solution at every trim iteration. Instead, the ΔC_l values that are required in the CAMRAD/JA trim loop are provided by computationally-fast two-dimensional tables of experimental data. Once the global iteration between CAMRAD/JA and FPR has converged, the ΔC_l values from the 2-D airfoil data go to zero and the lift values used for the CAMRAD/JA aerodynamic loads are completely provided by the three-dimensional unsteady CFD code. At this point, the calculation is considered to be fully converged and the CAMRAD/JA airfoil tables have been replaced by C_l values computed with the FPR code.

Note that after the FPR C_l values are brought into the CAMRAD/JA trim loop, they are modified with an unsteady correction that is derived from thin airfoil theory. The pitching moments, computed from 2-D airfoil tables, are also modified with a similar unsteady correction. These unsteady corrections are described in Ref. 12. The unsteady correction to C_l, was originally thought to be small and its effects on the CFD lift negligible. In this paper it will be shown that this is not necessarily the case for the Puma flight-test cases. The unsteady correction for moment is much more important and will also be examined in this paper.

For the Puma flight-test case 3, the iteration between CAMRAD/JA and FPR was considered converged after four runs with the CAMRAD/JA code and three runs with the FPR code. The results in the next section will investigate the effects of the iterative FPR coupling on the CAMRAD/JA solution.

Note that the airfoil sections used for the modified Puma blades are very similar to NACA 0012 sections but they are slightly thinner. Since no experimental airfoil data exists for these blades, the performance codes used NACA 0012 airfoil tables for their sectional aerodynamics. The CFD codes used the actual airfoil geometries in their calculations. The effects of this discrepancy are thought to be small and will be investigated further in follow-on work.

6. RESULTS AND DISCUSSION FOR THE COUPLED SOLUTION

Figure 9 shows some of the positive effects that the FPR computed lift has on the aerodynamic solution. Here the iteratively coupled FPR solution is compared with the initial uncoupled CAMRAD/JA solution and with the experimental data. The effects on the spanwise lift distribution are most clearly seen at 0° and 210°. At 0° there is a large spanwise flow toward the blade tip. Because of the large amount of blade sweep, this tends to make the area near the tip act like the trailing edge of an airfoil. Thus the lift drops abruptly near the tip as the pressure tries to reach stagnation. At 210° blade azimuth, the combined effects of blade sweep and spanwise flow tend to make the area near the blade tip act like the leading edge of an airfoil. Thus the flow expands along the upper surface and the lift is increased near the tip. This is clearly shown in the FPR solution and in the experimental data. The uncoupled CAMRAD/JA solution is based on two-dimensional airfoil tables with a tip-loss factor that always makes the lift go to zero at the blade tip. Thus the CAMRAD/JA solution cannot correctly model the three-dimensional lift increase at the blade tip near 180° azimuth.

The effects of the CFD coupling on the computed lift are shown in Fig. 10. Here the experimental data is shown as a heavy solid line in the figure. The initial CAMRAD/JA uncoupled solution is shown as a dotted line. The agreement is quite good with the experimental data. Next, the coupled FPR lift is shown as a dot-dash line. The agreement with experimental data is not as good as for the uncoupled CAMRAD/JA solution particularly at 0° and 180° blade azimuth. This was initially discouraging because one would think that the CFD lift should improve the solution. Finally it was discovered that the CAMRAD/JA code was taking the FPR lift solution and adding an unsteady correction factor to it as shown in the diagram in Fig. 8. This corrected value of lift is then used to compute the blade aerodynamic forces in the trim loop. This unsteady correction, based on thin airfoil theory, is not small as originally assumed. In fact, a fourth curve in Fig. 10, given by the dashed line, shows the lift values that the coupled CAMRAD/JA solution uses *after* it makes the unsteady lift correction. This line is very close to the initial uncoupled CAMRAD/JA solution and is in good agreement with the experimental data.

An obvious question regarding this situation is, "Why not simply remove the unsteady lift correction to the CFD code?" After all, the CFD codes should should

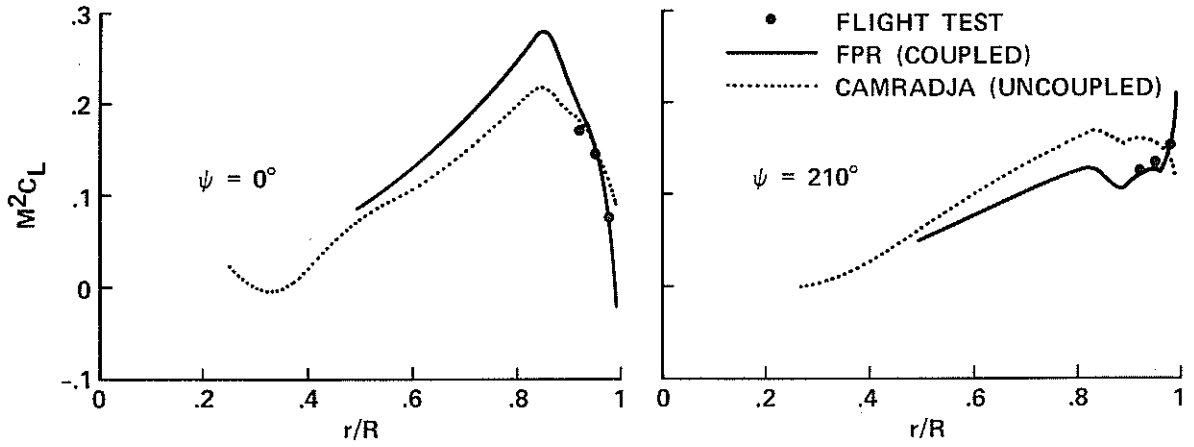

Fig. 9 Spanwise lift distributions at two azimuthal angles for the swept-tip Puma case 3.

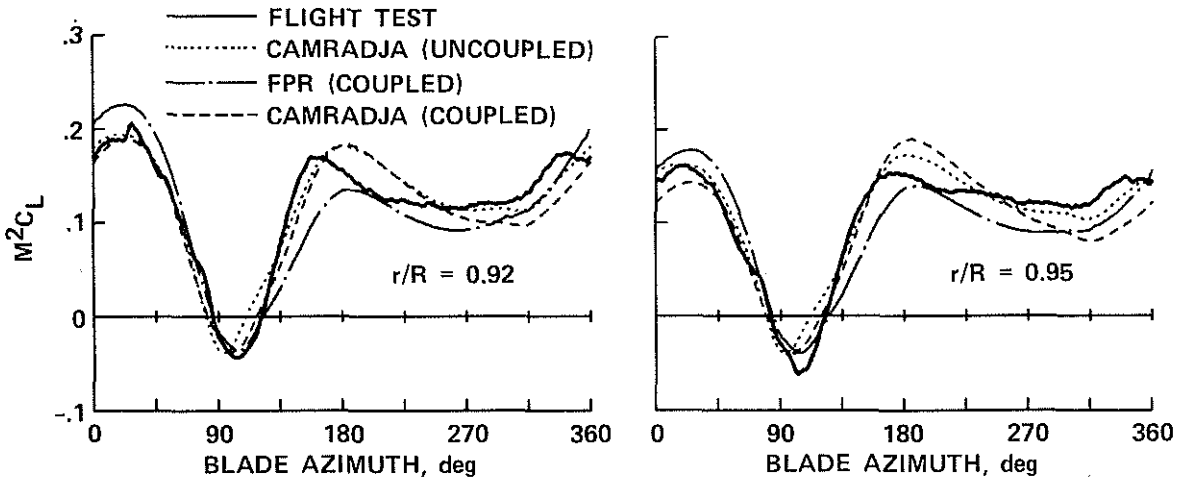

Fig. 10 A comparison of experimental and computed lift distributions for Puma flight-test case 3.

be able to correctly model any flowfield unsteadiness. It turns out that there are several problems with this line of reasoning. First, when the switch is used to turn off the unsteady lift correction in the CAMRAD/JA code, it also turns off the unsteady correction to the pitching moment. The unsteady correction for the pitching moment is very important for this Puma flight-test case and removing it would adversely affect the blade dynamics and trim.

The remaining problems with removing the unsteady lift correction in CAMRAD/JA are much more fundamental. If the unsteadiness has such an important effect on lift, then the CAMRAD/JA partial inflow angles do not convey adequate information to compute the unsteady effects. The CAMRAD/JA partial inflow angles lump together the unsteady effects of the rotor cyclic pitch, blade dynamics and wake inflow into a single inflow angle. The sum of the unsteadiness due to each of these separate unsteady mechanisms is *different* than the unsteadiness due to a single lumped partial angle. In other words, the correct boundary conditions for computing unsteady blade aerodynamics should include each of the blade lift mechanisms separately to the CFD code. The combined effects of cyclic pitch and torsion should be modeled as a local pitch effect. Blade flapping and bending should be treated as plunge, and the unsteady wake should be treated as a gust with distributed inflow over the blade surface. Separate tabular outputs for each of these effects need to be written by the performance codes and incorporated into the CFD boundary conditions.

A final point concerns the implementation of the boundary condition for pitch in the FPR code. The FPR code generates a grid about a zero angle-of-attack rotor section and then varies the sectional inflow angles with a transpiration boundary condition. This boundary condition is based on a quasi-steady assumption that says that the entire airfoil "sees" the same angle of attack at any given instant in time. It is not completely accurate for an unsteady pitching airfoil. Because the airfoil is pitching about the quarter chord, there is an unsteady effect that makes different chordwise sections of the airfoil experience slightly different angles of attack due to the unsteady pitch rate. For instance, if the airfoil is pitching nose-up, then the leading edge of the airfoil "sees" an additional negative inflow angle due to the unsteady motion and the trailing edge "sees" an additional positive angle of attack. Thus the FPR solution is time-accurate in the flowfield quantities and for plunge (this is still important for

transonic shock motion), but at present, the transpiration boundary condition does not accurately describe an unsteady pitching motion.

When the CFD codes were first coupled to CAMRAD by Tung et al. [5], the idea was mainly to include three-dimensional lift effects and unsteady transonics. Both of these can be adequately modeled with the current coupling scheme. They assumed that the low-speed unsteady effects were small because the reduced frequencies are typically low. For the Puma cases, the CAMRAD/JA solution says that the low-speed unsteady effects are important. If this is true, then the low-speed unsteady effects for lift and moment must be included properly in the CFD codes. It is relatively straightforward to put a rigorous unsteady surface boundary condition into the FPR code and we plan to do this as soon as possible. Guruswamy has already done this with a small-disturbance code and an Euler code in Refs. 21 and 22.

An illustration of how the unsteady effects of pitch are important is given in Fig. 11. The dominant term in the CAMRAD/JA unsteady lift and moment corrections is due to the blade cyclic pitching rate, $\dot{\theta}$. Fig. 11 shows that the local cyclic pitch rate at $r/R = 0.95$ is a maximum near 45° and 180° blade azimuth, roughly where the largest unsteady lift corrections are seen in Fig. 10. Also shown in Fig. 11 is the partial inflow angle that is provided as a boundary condition to the CFD code. The rate of change of the partial inflow angle is substantially less than that of the blade cyclic-pitch angle, particularly at 180° azimuthal angle. This illustrates the problem that the unsteadiness due to the sum of the lumped partial inflow angles will be different than the sum of each of the unsteady motion mechanisms. It also illustrates the second problem with the coupling scheme, that the FPR code does not contain the proper boundary condition to accurately include the unsteady pitching effects, even for the partial angles.

Figure 12 shows the computed results for pitching moment. Even though the CAMRAD/JA and FPR codes are coupled by the computed lift, there is no coupling between the two codes for pitching moment. Thus it is expected that the two codes will have different results for pitching moment, especially since the FPR solution has

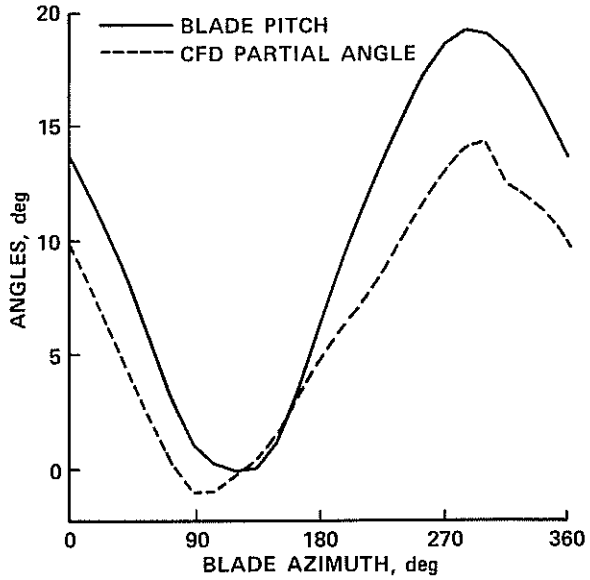

Fig. 11 Cyclic pitch and CAMRAD/JA partial angles of attack for Puma case 3 at $r/R = 0.95$.

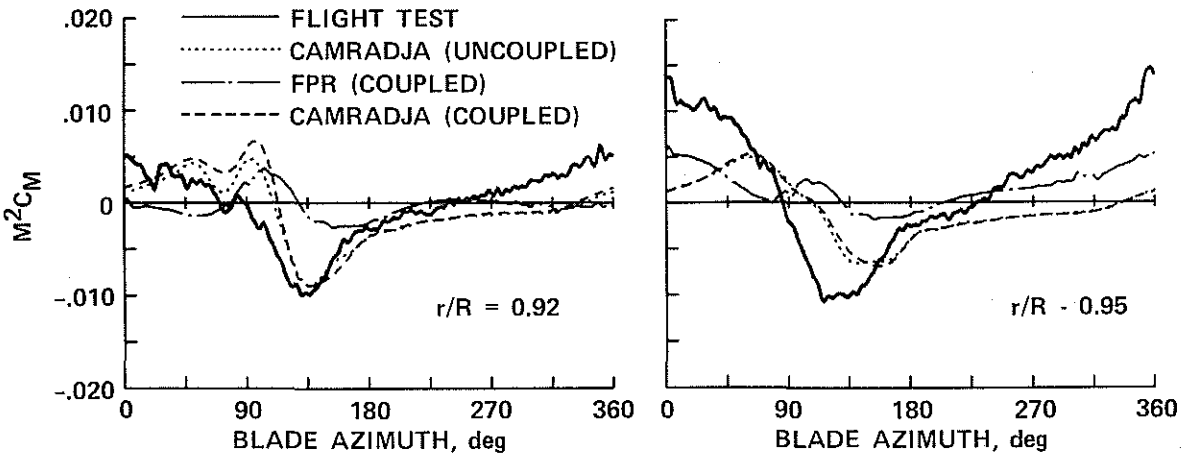

Fig. 12 A comparison of experimental and computed pitching moments for Puma flight-test case 3.

not included the viscous boundary-layer effects. This is indeed the case in Fig. 12. The coupled and uncoupled CAMRAD/JA results are very similar as was the case with the computed lift. They show reasonable agreement with the data, particularly at $r/R = 0.92$, but there is some phase lag at $r/R = 0.95$.

The FPR-computed moment is very different from the experimental data and also from the two CAMRAD/JA solutions. Rather than dismiss the FPR moments prediction as a poor calculation, it is useful to look at the influence of unsteady effects on the moment calculations. Figure 13 shows the same FPR and CAMRAD/JA moment results that are given in Fig. 12. A third result in Fig. 13 shows the CAMRAD/JA pitching moment that comes from the 2-D airfoil tables. The 2-D airfoil table result shows zero moment for most of the blade azimuth. It is only when it receives the unsteady correction in CAMRAD/JA that it takes on the large negative value in the second azimuthal quadrant and comes into better agreement with the experiment. Since it has already been stated that the boundary condition to the FPR code does not adequately convey the flowfield unsteadiness, then one cannot expect the CFD-computed pitching moment to agree with either the experimental data or the final

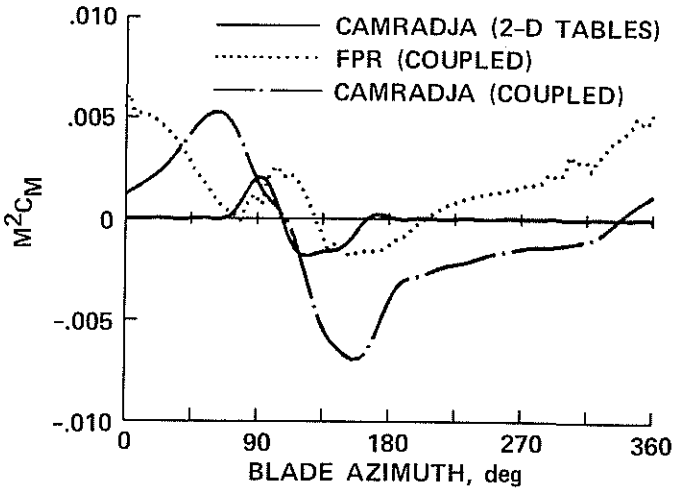

Fig. 13 A comparison of computed pitching moments for Puma flight-test case 3 at $r/R = 0.95$.

CAMRAD/JA result. In fact, the FPR pitching moment agrees better with the 2-D steady airfoil table result than it does with either the unsteady CAMRAD/JA result or the experimental data.

6. SUMMARY

A number of conclusions can be drawn from the coupled CAMRAD/JA and FPR results for this Puma swept-tip flight test. First, it is clear that the CFD coupling process is far from routine and that a meaningful solution must pay attention to the details of 1) the CFD solution, 2) the helicopter performance code, and 3) the coupling boundary condition between the two. The results in this paper have pointed out the need for a more accurate boundary condition between the helicopter performance codes and the CFD methods. The importance of accurately conveying unsteady information to the CFD codes is even more important if the CFD-computed drag and pitching moments are to be coupled to the performance codes.

The role of unsteadiness in the modeling of these flight-test cases casts a different light on some of the CFD results shown earlier in this paper. If the flowfield unsteadiness is important for lift and moment calculations, then the quasi-steady TSP code may not be suitable for coupled CFD and performance code calculations. Also, the disagreement of the three CFD codes on moment predictions is discouraging because the inclusion of significant flowfield unsteadiness will simply make these calculations more difficult.

In spite of these problems, it is clear that the CFD solutions offer details about the blade aerodynamics that cannot be provided by conventional helicopter performance codes. These details can be used in evaluating the relative effects of planform shape and airfoil section in rotor design. An example of this type of study is given by Scott et al. [23]. Also, the CFD aerodynamics makes the solution independent from the need for experimental 2-D airfoil tables. This paper has pointed out that there remains significant work to be done to accurately integrate the CFD codes into helicopter performance predictions. Hopefully it has also shown that a great deal of progress in CFD rotor predictions has been made to date and that this is expected to continue into the future.

7. ACKNOWLEDGEMENTS

The authors would like to thank Mr. John Bridgeman and Dr. Frank Caradonna of the U. S. Army Aeroflightdynamics Directorate (AFDD) for their helpful comments and discussion of this paper. Also, the efforts of Mr. William Bousman, also from the U. S. Army AFDD, are appreciated for developing a computer database for the computational and experimental data.

8. REFERENCES

1. Wayne Johnson, Development of a Comprehensive Analysis for Rotorcraft – I. Rotor Model and Wake Analysis, *Vertica*, vol. 5, 1981, pp. 99–130.
2. Wayne Johnson, Development of a Comprehensive Analysis for Rotorcraft – II. Aircraft Model, Solution Procedure and Applications, *Vertica*, vol. 5, 1981, pp. 185–216.
3. C. Young, "Development of the Vortex Ring Wake Model and Its Influence on the Prediction of Rotor Loads," *AGARD Conference Proceedings No. 334*, May 1982.
4. J. R. Van Gaasbeek, T. T. McLarty, and S. G. Sadler, "Rotorcraft Flight Simulation, Computer Program C81, Volume I – Engineer's Manual," USARTL TR77-54A, 1979.
5. C. Tung, F. X. Caradonna and W. Johnson, The Prediction of Transonic Flows on Advancing Rotors," *J. Am. Hel. Soc.*, Vol. 31, July, 1986, pp. 4-9.
6. G. K. Yamauchi, R. M. Heffernan, and M. Gaubert, "Correlation of SA349/2 Helicopter Flight Test DATA with a Comprehensive Rotorcraft Model," *NASA TM 88351* Feb. 1987.
7. R. C. Strawn and C. Tung, "Prediction of Unsteady Transonic Rotor Loads with a Full-Potential Rotor Code," *Presented at the 43rd Annual Forum of the American Helicopter Society*, May 18-20, 1987, St. Louis, MO.
8. I-Chung Chang, and C. Tung, "Numerical Solutions of the Full- Potential Equation for Rotors and Oblique Wings using a New Wake Model," AIAA Paper 85-0268, Jan. 1985.
9. Ki-Chung Kim and Inderjit Chopra, "Effects of Three-Dimensional Aeorodynamics on Blade Response and Loads," AIAA Paper 89-1285, April, 1989.
10. M. J. Riley and Judith V. Miller, "Pressure Distributions on a Helicopter Swept Tip from Flight Tests and from Calculations," Paper No. 9, *Presented at the Ninth European Rotorcraft Forum*, Sep 1983.
11. M. J. Riley, "Measurements of the Performance of a Helicopter Swept Tip Rotor in Flight," Paper No. 35, *Presented at the Twelfth European Rotorcraft Forum*, Sep 1986.
12. W. Johnson, "CAMRAD/JA; A Comprehensive Analytical Model of Rotorcraft Aerodynamics and Dynamics; Johnson Aeronautics Version; Volume I, Theory Manual," Johnson Aeronautics, Palo Alto, California, 1988.
13. J. Grant, "The Prediction of Supercritical Pressure Distributions on Blade Tips of Arbitrary Shape Over a Range of Advancing Blade Azimuth Angles," *Vertica*, 3, 1979, pp. 275–292.
14. F. X. Caradonna, and M. P. Isom, "Numerical Calculation of Unsteady Transonic Flow over Helicopter Rotor Blades," *AIAA J.* No. 4, April 1976.
15. J. J. Chattot, "Calculation of Three-Dimensional Unsteady Transonic Flow Past Helicopter Blades," NASA TP 1721, also AVRADCOM TR 80-A-2 (AM), 1980.
16. A. Desopper, "Study of the Unsteady Transonic Flow on Rotor Blades with Different Tip Shapes," *Vertica*, Vol. 9, 1985.
17. J. O. Bridgeman, J. L. Steger, and F. X. Caradonna, "A Conservative Finite-Difference Algorithm for the Unsteady Transonic Potential Equation in Generalized Coordinates," AIAA Paper No. 82-1388, August, 1982.
18. R. C. Strawn, and F. X. Caradonna, "Conservative Full-Potential Model for Unsteady Transonic Rotor Flows," *AIAA Journal* Vol. 25, No. 2, Feb. 1987, pp. 193-198.

19. J. O. Bridgeman, R. C. Strawn and F. X. Caradonna, "Advanced Rotor Computations with a Corrected Potential Method," *Presented at the 45th Annual Forum of the American Helicopter Society*, May 22-24, Boston, MA.
20. W. G. Bousman, C. Young, N. Gilbert, F. Toulmay, W. Johnson, and M. J. Riley, "Correlation of Puma Airloads – Lifting-Line and Wake Calculations," *Presented at the 15th European Rotorcraft Forum*, Amsterdam, The Netherlands, 12-15 Sept., 1989.
21. G. Guruswamy and T. Y. Yang, "Aeroelastic Time Response Analysis of Thin Airfoils by Transonic Code LTRAN2," *Computers and Fluids*, Vol. 9, No. 4, pp. 409-425.
22. G. Guruswamy, "Interaction of Fluids and Structures for Aircraft Applications," *Computers and Structures*, Vol. 30, No. 1/2, pp. 1-13, 1988
23. M. Scott, D. Sigl, and R. Strawn, "Computational and Experimental Evaluation of Helicopter Rotor Tips for High-Speed Forward Flight," AIAA paper 1845, *Presented at the AIAA 20th Fluid Dynamics, Plasma Dynamics and Lasers Conference*, Buffalo, New York, 12-14 June, 1989.